

# SEM: Enhancing Spatial Understanding for Robust Robot Manipulation

Xuewu Lin, Tianwei Lin, Lichao Huang, Hongyu Xie, Yiwei Jin, Keyu Li, Zhizhong Su\*

Robotics Laboratory, Horizon Robotics, Beijing, China

xuewu.lin@horizon.auto

## Abstract:

A key challenge in robot manipulation lies in developing policy models with strong spatial understanding—the ability to reason about 3D geometry, object relations, and robot embodiment. Existing methods often fall short: 3D point cloud models lack semantic abstraction, while 2D image encoders struggle with spatial reasoning. To address this, we propose **SEM** (Spatial Enhanced Manipulation model), a novel diffusion-based policy framework that explicitly enhances spatial understanding from two complementary perspectives. A spatial enhancer augments visual representations with 3D geometric context, while a robot state encoder captures embodiment-aware structure through graph-based modeling of joint dependencies. By integrating these modules, SEM significantly improves spatial understanding, leading to robust and generalizable manipulation across diverse tasks that outperform existing baselines.

**Keywords:** Robot Manipulation, Spatial Understanding, Diffusion Policy

## 1 Introduction

Robust robot manipulation in diverse real-world environments hinges on a core capability: spatial understanding, the ability to perceive and reason about 3D geometry, object relations, and the robot’s own embodiment. While recent diffusion-based policy models have demonstrated strong generative capacity for action modeling, their effectiveness remains limited by perceptual bottlenecks: (1) a reliance on 2D visual encoders with limited spatial reasoning, and (2) insufficient modeling of the robot’s internal structure beyond end-effector trajectories.

In this work, we propose **SEM** (Spatial Enhanced Manipulation model), a novel diffusion-based policy framework that explicitly enhances spatial understanding through two complementary perceptual modules. First, we introduce a **3D spatial enhancer** that lifts multi-view 2D image features into a unified 3D representation by leveraging camera geometry and depth observations. This module enables fine-grained spatial reasoning while preserving the semantic richness of 2D vision backbones, effectively resolving the spatial ambiguities inherent in purely 2D encodings. Second, we propose a **joint-centric robot state encoder** that models the robot’s kinematic structure as a graph of interconnected joints. By predicting distributions over full joint trajectories, not just end-effector poses, and applying graph attention to capture joint dependencies, this module enhances embodiment-aware understanding and enables finer-grained control.

By integrating these two modules into a unified diffusion transformer, SEM enhances action generation capabilities, improving both spatial understanding of the external environment and internal robot embodiment, resulting in more robust, generalizable, and precise manipulation.

We extensively evaluate SEM in both simulation and real-world environments. On the RoboTwin benchmark, which includes 16 dual-arm manipulation tasks, SEM outperforms competitive baselines by 22.1%, achieving state-of-the-art performance. Additional experiments show strong generalization to new camera viewpoints and robot configurations, while real-world deployments validate its effectiveness in physical settings. Our contributions are threefold:

- We introduce SEM, a novel diffusion-based policy framework that centers on spatial understanding as the core design principle for robot manipulation.
- We introduce two key modules: a spatial enhancer to unify 2D visual features in 3D space, and a joint-centric state encoder to model full-robot dynamics via graph attention.
- We demonstrate that SEM achieves state-of-the-art performance on the RoboTwin benchmark and generalizes well to real-world settings.

## 2 Related Works

The development of end-to-end manipulation algorithms for robots is progressing rapidly, with analyses and improvements being made from various perspectives.

Early research efforts [1, 2, 3, 4] leverage imitation learning to acquire the ability to solve complex tasks based on human demonstrations, achieving remarkable success. Subsequently, some studies focus on refining the action distribution model of imitation learning to enhance training stability and performance, including implicit model [5], mixture of gaussians [6] and diffusion policy [7].

Moreover, numerous studies [8, 9, 10] have contributed to the improvement of algorithmic pipelines and network architectures. The 3D Diffuser Actor [11] combines elements from both Act3D and diffusion policy [7], resulting in a significant enhancement. RVT [12] re-renders input images onto three orthogonal planes using virtual cameras, ultimately outputting heatmaps to represent the EE poses of keyframes. RVT-2 [13] builds on RVT by introducing a fine branch, further improving action precision. KStarDiffuser [14] designs a novel model aimed at addressing complex dual-arm tasks, utilizing graph convolution networks to encode the historical trajectories of robotic arms and incorporating joint position loss to constrain the predictions. The aforementioned methods predict the next keyframe’s EE pose, which limits their suitability for more intricate tasks such as folding clothes. To address this, DP3 [15] directly employs a diffusion policy to output joint positions.

In the past two years, breakthroughs in VLMs [16, 17, 18, 19] have spurred growing research interest in generalist action models. These models [20, 21, 22, 23, 24, 25, 26] use VLMs as the base model and are trained on diverse embodied intelligence datasets with the aim to achieve high levels of scenario, embodiment, and task generalization. There are some methods that improve VLMs to better integrate into embodied tasks, such as SpatialVLA [27] which incorporates 3D position embedding into VLMs. Although these VLM-based models have made notable progress, they still exhibit performance limitations when applied in real-world scenarios.

This paper focuses more on the network design of the action model, equipping the model with better 3D understanding capabilities, rather than concentrating on VLM-based generalist models. Noteworthy, the approaches most closely related to our method, SEM, are KStarDiffuser [14] and SpatialVLA [27]. Unlike SEM, both methods output EE poses instead of joint positions and show notable differences in network architecture. Moreover, SpatialVLA does not account for extrinsic camera parameters, which restricts its capability to process only a single-view image.

## 3 Problem Formulation

The inputs for the manipulation problem primarily consist of sensor data and current joint positions  $\mathbf{S}$ , where sensor data generally encompass multi-view images  $\mathbf{I}$  and depth maps  $\mathbf{D}$ . To simplify the problem, this paper utilizes only the sensor data from the current frame. When handling multitask, instruction texts  $\mathbf{T}$  are required as well. Moreover, we consider modeling both the camera and the embodiment structure, thus requiring inputs of camera parameters  $\mathbf{C}$  and embodiment structure parameters  $\mathbf{E}$ . Thus, the inputs can be summarized into the following parts:

$$\text{Input} = \{\mathbf{I} \in \mathbb{R}^{N \times H \times W \times 3}, \mathbf{D} \in \mathbb{R}^{N \times H \times W \times 1}, \mathbf{S} \in \mathbb{R}^{N_j}, \mathbf{T}\} \cup \{\mathbf{C}, \mathbf{E}\} \quad (1)$$

Here,  $N$  represents the number of images,  $N_j$  denotes the number of joints.  $\mathbf{C}$  and  $\mathbf{E}$  can be abstracted as the camera’s projection function and the embodiment’s kinematics function, respec-

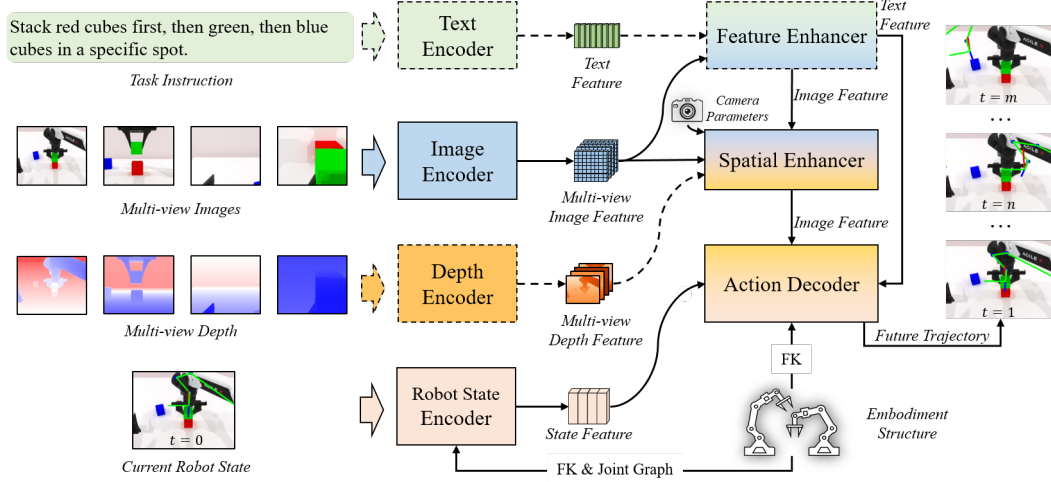


Figure 1: The overall architecture of SEM, where dashed lines indicate plug-and-play components. SEM takes image, depth, current robot state, and instruction as inputs, and performs end-to-end prediction of future joint positions. SEM can fully leverage camera and embodiment parameters to enhance model performance and generalization.

tively. The output of this problem is the robot joint positions for the next  $t_{out}$  frames, denoted as  $\mathbf{S}_{out} \in \mathbb{R}^{N_j \times t_{out}}$ .

## 4 Our Method: SEM

The overall architecture of SEM is illustrated in Figure 1, comprising seven sub-modules: a text encoder for encoding instructions; an image encoder and a depth encoder that convert visual inputs into high-dimensional feature maps; a feature enhancer for fusing text and image features (Section 4.1); a spatial enhancer that injects spatial and geometric awareness into image features (Section 4.2); a robot state encoder used for encoding the robot’s historical trajectory  $\mathbf{S}$  (Section 4.3); and an action decoder that predicts future trajectories  $\mathbf{S}_{out}$  from the aggregated features (Section 4.4).

### 4.1 Feature Enhancer

The feature enhancer enables cross-modal fusion and alignment of text and image features, while emphasizing task-relevant regions. We explore two implementations: a GroundingDINO-style enhancer [28] and a language model-style enhancer. As illustrated in Fig.2(a), the GroundingDINO-style enhancer employs bidirectional cross-attention for text-image interaction, along with deformable self-attention for image features and vanilla self-attention for text features. In contrast, the language model-style enhancer, which is commonly used in action models [20, 21, 27], treats both image and text features as token sequences that are directly input into a language model, as shown in Fig. 2(b). This approach provides stronger multimodal understanding and generally yields better feature enhancement, but at the cost of reduced computational efficiency.

### 4.2 Spatial Enhancer

To effectively leverage both rich 2D image features and accurate 3D geometric information, we design a spatial enhancer within SEM. In multi-view feature fusion tasks such as 3D detection, a common practice (BEVDet, BIP3D [29]) is to aggregate features based on sampled points along the camera frustum. Inspired by this, our spatial enhancer integrates multi-view 2D image features with depth-aware 3D representations to enhance 3D spatial understanding.

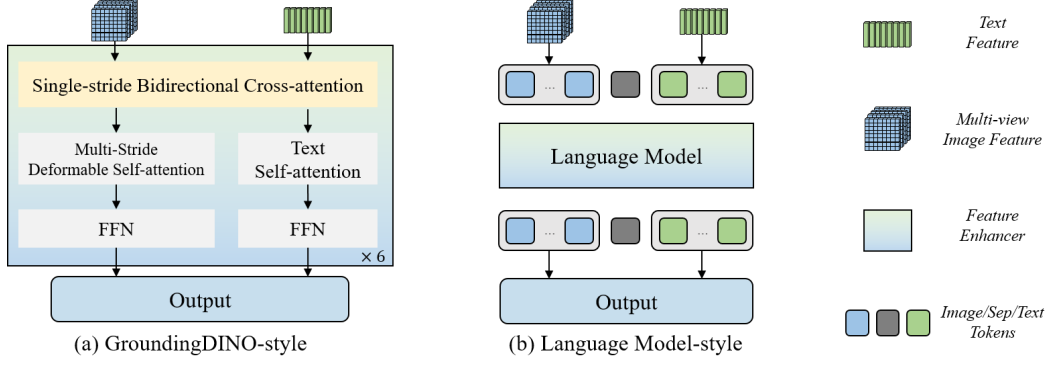


Figure 2: Two different styles of the feature enhancer.

In this work, the proposed spatial enhancer performs two critical functions: (1) establishing a camera model to project 2D image features into 3D space, and (2) fusing image features with depth features to produce representations with stronger geometric awareness. As illustrated in Fig. 3(a), the enhancer takes multi-view image features, depth features, and camera parameters as input, and outputs enhanced features with better spatial understanding. Specifically, for each image feature: (1) a set of depth values is sampled, and the corresponding pixel coordinates are projected into 3D space using the camera model. These 3D coordinates are then encoded into high-dimensional embeddings; (2) a discrete depth distribution is predicted and used to compute a weighted sum over these 3D embeddings, resulting in a 3D positional embedding for each image feature. Finally, the image feature, depth feature, and 3D positional embedding are fused via a simple MLP.

To support depth sensor-free scenarios, the depth feature is designed as pluggable (the dashed parts in Fig. 3(a)). If without depth input, we directly predict depth distribution based on image feature. We select the base coordinate system of the embodiment for performing the 3D encoding, unifying all multi-view features into this coordinate system. Subsequent 3D encoding for the embodiment will also be conducted in the same coordinate system, as described in Section 4.3 and Section 4.4.

### 4.3 Robot State Encoder

The robot state encoder is used to encode the current robot state  $\mathbf{S}$ . We first use forward kinematics to compute the 6D pose of each joint in the robot base coordinate system and then integrate it with the joint positions to obtain  $\mathbf{S}'$ .

$$\mathbf{S}' \in \mathbb{R}^{N_j \times 8}, \mathbf{S}'_{i,j} = [a, x, y, z, q_w, q_x, q_y, q_z]_{i,j} \quad (2)$$

where  $a$  is the joint position,  $[x, y, z]$  represents the 3D coordinates of the joint, and  $[q_w, q_x, q_y, q_z]$  denotes the rotation quaternion. We first project the feature  $\mathbf{S}'$  into a high-dimensional space using an MLP, then feed it into a transformer encoder with joint graph attention as its core component. The joint graph attention utilizes the joint distance matrix  $\mathbf{J} \in \mathbb{R}^{N_j \times N_j}$  to encode relative positions, where each entry  $\mathbf{J}_{i,j}$  denotes the number of links between the  $i_{th}$  query joint and the  $j_{th}$  key joint. The formulation is as follows.

$$\mathbf{P} = \text{MLP}(\text{SinCos}(\mathbf{J})) \in \mathbb{R}^{N_j \times N_j \times d} \quad (3)$$

$$\mathbf{A} = \text{einsum}(ik, ijk, jk \rightarrow ij | \mathbf{Q}, \mathbf{P}, \mathbf{K}) \in \mathbb{R}^{N_j \times N_j} \quad (4)$$

$$\mathbf{O} = \text{softmax}\left(\frac{\mathbf{A}}{\sqrt{d}}\right) \mathbf{V} \quad (5)$$

where  $\mathbf{Q}$ ,  $\mathbf{K}$ ,  $\mathbf{V}$  and  $\mathbf{O}$  denote query, key, value and output features,  $d$  is the feature channels, and  $\text{einsum}$  is the Einstein summation convention. For simplicity, we have omitted the head dimension here. It is important to note that the computational complexity of joint graph attention is  $O(N_j^2 d^2)$ , which is higher than vallina attention's  $O(N_j^2 d + N_j d^2)$ . However, since  $N_j$  is typically small, the computational load of this module is not a bottleneck.

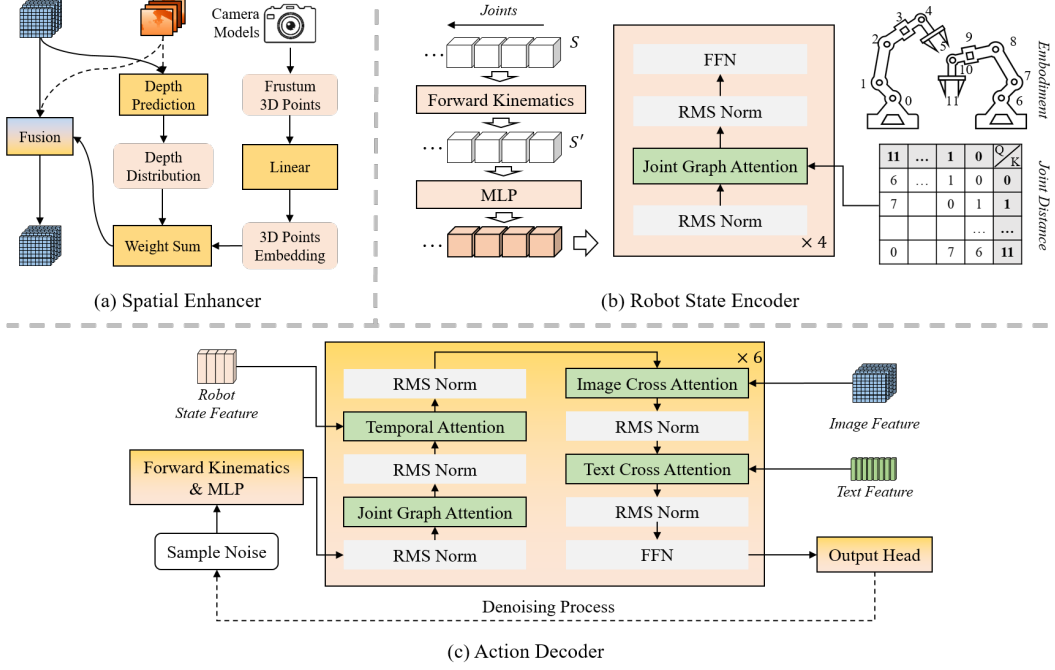


Figure 3: Network structure of the spatial enhancer, robot state encoder and action decoder.

#### 4.4 Action Decoder

The action decoder takes all condition features as input and employs a diffusion transformer to predict future trajectories. We begin by applying noise to the joint positions and use forward kinematics to obtain a noisy robot state  $\mathbf{S}'_{out} \in \mathbb{R}^{N_j \times tout \times 8}$ , ensuring that it remains consistent with the robot's embodied structure. The transformer decoder then processes this noisy state, producing the denoised prediction  $\mathbf{S}'_{out}$  through an output head. Compared to the robot state encoder, the action decoder includes three additional cross-attention modules, each attending to robot state, image, and text features respectively (see Fig. 3(c)). Temporal cross-attention operates in a causal manner, ensuring unidirectional flow along the time axis. Finally, an output head composed of upsampling and 1D convolution layers generates the structured prediction.

#### 4.5 Training Loss

During training, we employ four loss components: joint position loss, joint pose loss, forward kinematics pose loss, and depth loss, as defined in Equation 6. The joint position loss  $L_{joint}$  and joint pose loss  $L_{pose}$  are defined as the L1 distances between the predicted joint angles and 6D poses and their corresponding ground truths. To further enhance positional accuracy, the forward kinematics pose loss  $L_{pose}^{fk}$  recalculates 6D poses from the predicted joint positions using forward kinematics and compares them with the ground truth via an additional L1 distance. In contrast to prior methods, our approach constrains both joint angles and 6D poses, providing stronger supervisory signals. This richer supervision leads to improved performance. The depth loss  $L_{depth}$ , applied to the depth distribution predicted by the spatial enhancer, is formulated as a cross-entropy loss.

$$L = \lambda_1 L_{joint} + \lambda_2 L_{pose} + \lambda_3 L_{pose}^{fk} + \lambda_4 L_{depth} \quad (6)$$

	Hammer Beat	Block Handover	Bottle Adjust	Blocks Stack (easy/hard)
DP3	82.0±6.6	85.3±14.5	42.0±7.0	44.7±1.2 / 6.3±3.1
DP	0.0±0.0	76.0±16.1	35.7±2.9	8.0±4.4 / 0.3±0.6
SEM	97.0±1.4	96.7±1.2	69.0±5.1	76.3±2.6 / 89.7±1.7
SEM-GD	38.3±1.7	78.7±2.6	16.7±1.24	85.0±0.8 / 69.3±4.9
SEM-QW	95.3±2.1	79.7±2.1	68.7±4.7	69.7±4.2 / 47.0±4.2
	Container Place	Bottles Pick	Dual Shoes Place	Dual Bottles Pick (easy/hard)
DP3	62.3±6.8	14.7±4.7	6.0±1.0	75.7±17 / 55.7±4.9
DP	14.0±6.9	12.0±5.3	3.0±1.0	85.7±6.7 / 59.3±5.5
SEM	56.3±4.2	56.3±5.3	51.7±2.6	98.0±0.8 / 60.7±0.5
SEM-GD	52.7±4.5	58.3±3.7	39.0±8.6	98.0±0.8 / 67.3±0.9
SEM-QW	72.0±0.8	61.0±6.5	64.3±2.5	98.7±1.2 / 62.7±3.9
	Empty Cup Place	Pick Apple	Put Apple Cabinet	Mug hanging (easy/hard)
DP3	81.0±2.6	54.0±12.8	78.3±3.8	3.0±1.0 / 2.3±2.5
DP	87.7±0.6	29.3±5.0	8.0±12.2	0.0±0.0 / 0.0±0.0
SEM	87.0±2.2	98.7±0.5	73.3±0.9	12.3±4.8 / 6.0±1.6
SEM-GD	63.7±2.5	80.0±2.2	37.0±1.4	2.7±0.5 / 3.0±0.8
SEM-QW	85.7±1.2	90.3±3.7	32.7±4.7	2.3±0.5 / 3.7±1.2
	Shoe Place		Mean	
DP3	54.0±11.5		46.7±6.2	
DP	33.0±15.8		28.3±5.2	
SEM	88.3±1.2		69.8±2.7	
SEM-GD	73.0±1.6		53.9±2.4	
SEM-QW	87.7±2.6		63.8±2.9	

Table 1: RoboTwin Benchmark Results. DP3, DP, and SEM are single-task models, while SEM-GD and SEM-QW are multi-task. SEM-GD uses a GroundingDINO-style enhancer with GroundingDINO-Tiny as backbone. SEM-QW adopts a language model-style enhancer based on Qwen2.5-VL, with its parameters frozen during training.

#### 4.6 Implementation

To improve generalization to camera parameters, we apply a camera intrinsic standardization preprocessing step. Given the origin camera intrinsics  $C_I'$  and a predefined standardized camera intrinsics  $C_I''$ , we transform the input image via inverse projection  $C_I'^{-1}(C_I''(i, j, 1))$ , where  $(i, j, 1)$  are the unit-depth pixel coordinates.

Our experiments involve three distinct models: (1) Single-task model: Trained and evaluated on a single task, without text encoder and feature enhancer, using Swin-Transformer-Tiny [30] as the image encoder; (2) GroundingDINO-style multi-task model: Employs the GroundingDINO-style feature enhancer with GroundingDINO-Tiny [28] as the base model; (3) Language model-style multi-task model: Utilizes Qwen2.5-VL [31] as the base model, with all Qwen-VL parameters frozen during training. More implementation details are provided in the appendix.

## 5 Experiments

We conducted experiments in both simulation and real-world settings. Simulation experiments are performed using the RoboTwin benchmark [32], built on the SAPIEN simulator and consisting of 16 bimanual manipulation tasks. For real-world experiments, we selected 4 representative tasks from the benchmark. Unless otherwise specified, each task was trained with 100 demonstrations. All tasks adopted closed-loop success rate as the evaluation metric.

### 5.1 Main Results on Simulation

We first compare our method with existing approaches (DP3 [15] and DP [7]) under the single-task setting on the RoboTwin benchmark. DP3 uses color point clouds as input. As shown in Tab. 1,

Train	Test	Blocks Stack Hard	Dual Bottles Pick Hard	Block Handover
EXT0[100]	EXT0	89.7 $\pm$ 1.7	60.7 $\pm$ 0.5	96.7 $\pm$ 1.2
EXT0[100]	EXT1	9.3 $\pm$ 2.4	43.0 $\pm$ 1.4	41.0 $\pm$ 4.5
EXT1[20]	EXT1	1.3 $\pm$ 0.5	31.0 $\pm$ 3.6	64.3 $\pm$ 5.4
EXT0[100] $\rightarrow$ EXT1[20]	EXT1	62.3 $\pm$ 2.9	49.0 $\pm$ 0.8	97.3 $\pm$ 1.2
Train	Test	Shoe Place	Empty Cup Place	Mean
EXT0[100]	EXT0	88.3 $\pm$ 1.2	87 $\pm$ 2.2	84.5 $\pm$ 1.3
EXT0[100]	EXT1	47.7 $\pm$ 2.1	36.3 $\pm$ 4.1	35.5 $\pm$ 2.9
EXT1[20]	EXT1	44.3 $\pm$ 3.4	23.7 $\pm$ 1.2	33.1 $\pm$ 2.8
EXT0[100] $\rightarrow$ EXT1[20]	EXT1	81.7 $\pm$ 2.1	65.3 $\pm$ 3.4	71.1 $\pm$ 2.1

Table 2: Experimental results of extrinsic generalization. EXT0[100] and EXT1[20] represent datasets with 100 samples of extrinsic parameters EXT0 and 20 samples of extrinsic parameters EXT1 respectively. EXT0[100] $\rightarrow$ EXT1[20] denotes pre-training on EXT0[100] followed by fine-tuning on EXT1[20].

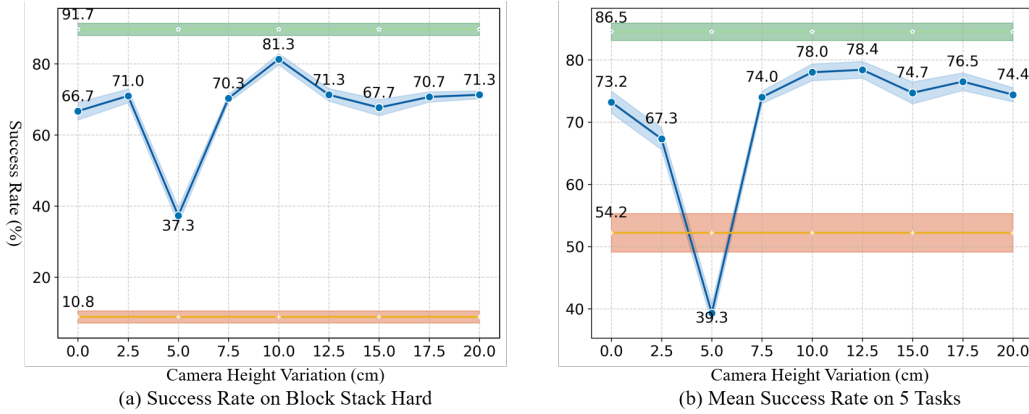


Figure 4: Experimental results of training and generalization with mixed multi-extrinsic data. The orange and green regions represent the upper and lower reference bounds respectively.

SEM achieves significant performance gains, with average success rate improvements of 22.1% over DP3 and 41.5% over DP. Notably, SEM demonstrates especially strong performance on tasks requiring high-precision manipulation, achieving an 89.7% success rate on the Block Stack Hard task, compared to 6.3% (DP3) and 0.3% (DP). To further validate the effectiveness of our policy in multi-task scenarios, we integrate it with two 2D vision foundation models: GroundingDINO-Tiny and Qwen2.5-VL. GroundingDINO-Tiny achieves an average success rate of 53.9%. Remarkably, Qwen2.5-VL, even with its parameters frozen during training, reaches an average success rate of 63.8%, approaching single-task model performance.

## 5.2 Camera Generalization

The generalization capability of camera parameters reflects the model’s 3D understanding and overall generalization prowess. We conducted three sets of experiments to assess this.

Firstly, we evaluate the model’s ability to generalize across different camera extrinsics. Specifically, we assess whether high performance can be achieved on a new camera setup using only a small amount of adaptation data. The experiment considers two extrinsic configurations (EXT0 and EXT1), differing by a 10cm height offset. As shown in Tab. 2, SEM exhibits a degree of zero-shot generalization, attaining a 35.5% success rate on EXT1 when trained solely on EXT0. With just 20 samples from EXT1 for fine-tuning, performance improves significantly to 71.1%, substantially outperforming the 33.1% success rate of training from scratch.



Setting	Blocks Stack Hard	Dual Bottles Pick Hard	Block Handover
SEM	89.7 $\pm$ 1.7	60.7 $\pm$ 0.5	96.7 $\pm$ 1.2
RGB-only	80.7 $\pm$ 2.9	55.3 $\pm$ 0.5	95.0 $\pm$ 2.4
Without Spatial Enhancer	76.3 $\pm$ 4.6	53.7 $\pm$ 1.9	86.7 $\pm$ 4.2
MLP State Encoder	41.7 $\pm$ 3.9	54.3 $\pm$ 1.7	94.0 $\pm$ 1.6
Setting	Shoe Place	Empty Cup Place	Mean
SEM	88.3 $\pm$ 1.2	87 $\pm$ 2.2	84.5 $\pm$ 1.4
RGB-only	86.3 $\pm$ 3.3	92.7 $\pm$ 0.5	82.0 $\pm$ 1.9
Without Spatial Enhancer	79.3 $\pm$ 2.9	87.3 $\pm$ 3.3	76.7 $\pm$ 3.4
MLP State Encoder	88.3 $\pm$ 3.9	86.3 $\pm$ 0.5	72.9 $\pm$ 2.3

Table 3: Ablation Study Results On RoboTwin Benchmark.

Secondly, we tested the model’s ability to generalize directly to new camera extrinsic parameters when trained on mixed multi-group extrinsic data. The model was trained on three groups with camera height variations of 0cm, 10cm, and 20cm (33 samples per group). Testing across heights from 0-20cm, the model maintained over 70% success on average and on the challenging ‘Blocks Stack Hard’ task (Fig. 4). This outperformed the lower bound of training with only 33 samples and approached the upper limit achieved by training with 100 samples for a single extrinsic parameter. An outlier at 5cm suggests a non-linear relationship between extrinsic parameters and success rate, which requires further analysis. Intrinsic generalization experiments are in the appendix.

### 5.3 Ablation Study

Tab. 3 summarizes our ablation experiments on SEM, demonstrating the impact of individual components: (1) Without depth input, the average success rate remains at 82.0%, yet the Block Stack Hard task experiences a performance reduction of 9.0 percentage points (from 89.7% to 80.7%). (2) Eliminating the spatial enhancer results in a 7.8 percentage point decrease in the average success rate across five tasks (from 84.5% to 76.7%). (3) Replacing the robot state encoder with a simple MLP leads to a substantial 11.6 percentage point drop in the average success rate (to 72.9%), with the Block Stack Hard task suffering a significant 48.0 percentage point decrease (to 41.7%).

### 5.4 Real World Performance

We conducted real-world experiments on four tasks, training each with 100 demonstrations. Due to significant differences between our manipulator and the RoboTwin simulator, we abandoned the sim2real transfer and instead trained from scratch. The experiment results are shown in Tab. 4, proving our method can also achieve good performance in real-world settings.

	Empty Cup Place	Shoe Place	Block Stack Easy	Diverse Bottles Pick
SEM	41 / 50	38 / 50	26 / 50	27 / 50

Table 4: Success Rate of Real World Experiments.

## 6 Conclusion

We introduced **SEM**, a diffusion-based policy framework that improves robot manipulation by enhancing spatial understanding. By incorporating a 3D spatial enhancer and a joint-centric robot state encoder, SEM enables better reasoning of both external geometry and the robot’s internal structure. SEM achieves state-of-the-art performance on the RoboTwin benchmark and demonstrates camera generalization capability through experiments. Real-world experiments also yield promising results. We partially demonstrate the importance of spatial understanding in advancing robot manipulation policy learning. Our method still has significant room for optimization, and we plan to conduct larger-scale training for general multi-task policy model in the future.



## References

- [1] D. A. Pomerleau. Alvin: An autonomous land vehicle in a neural network. *Advances in neural information processing systems*, 1, 1988.
- [2] F. Torabi, G. Warnell, and P. Stone. Behavioral cloning from observation. In *Proceedings of the Twenty-Seventh International Joint Conference on Artificial Intelligence*. International Joint Conferences on Artificial Intelligence Organization, 2018.
- [3] T. Zhang, Z. McCarthy, O. Jow, D. Lee, X. Chen, K. Goldberg, and P. Abbeel. Deep imitation learning for complex manipulation tasks from virtual reality teleoperation. In *2018 IEEE international conference on robotics and automation (ICRA)*, pages 5628–5635. Ieee, 2018.
- [4] A. Zeng, S. Song, J. Lee, A. Rodriguez, and T. Funkhouser. Tossingbot: Learning to throw arbitrary objects with residual physics. *IEEE Transactions on Robotics*, 36(4):1307–1319, 2020.
- [5] P. Florence, C. Lynch, A. Zeng, O. A. Ramirez, A. Wahid, L. Downs, A. Wong, J. Lee, I. Mor-datch, and J. Tompson. Implicit behavioral cloning. In *Conference on robot learning*, pages 158–168. PMLR, 2022.
- [6] N. M. Shafiullah, Z. Cui, A. A. Altanzaya, and L. Pinto. Behavior transformers: Cloning  $k$  modes with one stone. *Advances in neural information processing systems*, 35:22955–22968, 2022.
- [7] C. Chi, Z. Xu, S. Feng, E. Cousineau, Y. Du, B. Burchfiel, R. Tedrake, and S. Song. Diffusion policy: Visuomotor policy learning via action diffusion. *The International Journal of Robotics Research*, page 02783649241273668, 2023.
- [8] T. Z. Zhao, V. Kumar, S. Levine, and C. Finn. Learning fine-grained bimanual manipulation with low-cost hardware. *arXiv preprint arXiv:2304.13705*, 2023.
- [9] M. Shridhar, L. Manuelli, and D. Fox. Perceiver-actor: A multi-task transformer for robotic manipulation. In *Conference on Robot Learning*, pages 785–799. PMLR, 2023.
- [10] T. Gervet, Z. Xian, N. Gkanatsios, and K. Fragkiadaki. Act3d: 3d feature field transformers for multi-task robotic manipulation. *arXiv preprint arXiv:2306.17817*, 2023.
- [11] T.-W. Ke, N. Gkanatsios, and K. Fragkiadaki. 3d diffuser actor: Policy diffusion with 3d scene representations. In *8th Annual Conference on Robot Learning*, 2024.
- [12] A. Goyal, J. Xu, Y. Guo, V. Blukis, Y.-W. Chao, and D. Fox. Rvt: Robotic view transformer for 3d object manipulation. In *Conference on Robot Learning*, pages 694–710. PMLR, 2023.
- [13] A. Goyal, V. Blukis, J. Xu, Y. Guo, Y.-W. Chao, and D. Fox. Rvt-2: Learning precise manipulation from few demonstrations. *arXiv preprint arXiv:2406.08545*, 2024.
- [14] Q. Lv, H. Li, X. Deng, R. Shao, Y. Li, J. Hao, L. Gao, M. Y. Wang, and L. Nie. Spatial-temporal graph diffusion policy with kinematic modeling for bimanual robotic manipulation. *arXiv preprint arXiv:2503.10743*, 2025.
- [15] Y. Ze, G. Zhang, K. Zhang, C. Hu, M. Wang, and H. Xu. 3d diffusion policy. *arXiv e-prints*, pages arXiv–2403, 2024.
- [16] X. Chen, J. Djolonga, P. Padlewski, B. Mustafa, S. Changpinyo, J. Wu, C. R. Ruiz, S. Goodman, X. Wang, Y. Tay, et al. Pali-x: On scaling up a multilingual vision and language model. *arXiv preprint arXiv:2305.18565*, 2023.
- [17] H. Liu, C. Li, Q. Wu, and Y. J. Lee. Visual instruction tuning. *Advances in neural information processing systems*, 36:34892–34916, 2023.

- [18] L. Beyer, A. Steiner, A. S. Pinto, A. Kolesnikov, X. Wang, D. Salz, M. Neumann, I. Alabdulmohsin, M. Tschanen, E. Bugliarello, et al. Paligemma: A versatile 3b vlm for transfer. *arXiv preprint arXiv:2407.07726*, 2024.
- [19] P. Wang, S. Bai, S. Tan, S. Wang, Z. Fan, J. Bai, K. Chen, X. Liu, J. Wang, W. Ge, et al. Qwen2-vl: Enhancing vision-language model’s perception of the world at any resolution. *arXiv preprint arXiv:2409.12191*, 2024.
- [20] M. J. Kim, K. Pertsch, S. Karamcheti, T. Xiao, A. Balakrishna, S. Nair, R. Rafailov, E. Foster, G. Lam, P. Sanketi, et al. Openvla: An open-source vision-language-action model. *arXiv preprint arXiv:2406.09246*, 2024.
- [21] K. Black, N. Brown, D. Driess, A. Esmail, M. Equi, C. Finn, N. Fusai, L. Groom, K. Hausman, B. Ichter, et al. pi0: A vision-language-action flow model for general robot control. *arXiv preprint arXiv:2410.24164*, 2024.
- [22] S. Liu, L. Wu, B. Li, H. Tan, H. Chen, Z. Wang, K. Xu, H. Su, and J. Zhu. Rdt-1b: a diffusion foundation model for bimanual manipulation. *arXiv preprint arXiv:2410.07864*, 2024.
- [23] O. M. Team, D. Ghosh, H. Walke, K. Pertsch, K. Black, O. Mees, S. Dasari, J. Hejna, T. Kreiman, C. Xu, et al. Octo: An open-source generalist robot policy. *arXiv preprint arXiv:2405.12213*, 2024.
- [24] J. Wen, M. Zhu, Y. Zhu, Z. Tang, J. Li, Z. Zhou, C. Li, X. Liu, Y. Peng, C. Shen, et al. Diffusion-vla: Scaling robot foundation models via unified diffusion and autoregression. *arXiv preprint arXiv:2412.03293*, 2024.
- [25] A. O’Neill, A. Rehman, A. Maddukuri, A. Gupta, A. Padalkar, A. Lee, A. Pooley, A. Gupta, A. Mandlekar, A. Jain, et al. Open x-embodiment: Robotic learning datasets and rt-x models: Open x-embodiment collaboration 0. In *2024 IEEE International Conference on Robotics and Automation (ICRA)*, pages 6892–6903. IEEE, 2024.
- [26] X. Li, P. Li, M. Liu, D. Wang, J. Liu, B. Kang, X. Ma, T. Kong, H. Zhang, and H. Liu. Towards generalist robot policies: What matters in building vision-language-action models. *arXiv preprint arXiv:2412.14058*, 2024.
- [27] D. Qu, H. Song, Q. Chen, Y. Yao, X. Ye, Y. Ding, Z. Wang, J. Gu, B. Zhao, D. Wang, et al. Spatialvla: Exploring spatial representations for visual-language-action model. *arXiv preprint arXiv:2501.15830*, 2025.
- [28] S. Liu, Z. Zeng, T. Ren, F. Li, H. Zhang, J. Yang, Q. Jiang, C. Li, J. Yang, H. Su, et al. Grounding dino: Marrying dino with grounded pre-training for open-set object detection. In *European Conference on Computer Vision*, pages 38–55. Springer, 2024.
- [29] X. Lin, T. Lin, L. Huang, H. Xie, and Z. Su. Bip3d: Bridging 2d images and 3d perception for embodied intelligence. *arXiv preprint arXiv:2411.14869*, 2024.
- [30] J. Su, M. Ahmed, Y. Lu, S. Pan, W. Bo, and Y. Liu. Roformer: Enhanced transformer with rotary position embedding. *Neurocomputing*, 568:127063, 2024.
- [31] S. Bai, K. Chen, X. Liu, J. Wang, W. Ge, S. Song, K. Dang, P. Wang, S. Wang, J. Tang, et al. Qwen2. 5-vl technical report. *arXiv preprint arXiv:2502.13923*, 2025.
- [32] Y. Mu, T. Chen, S. Peng, Z. Chen, Z. Gao, Y. Zou, L. Lin, Z. Xie, and P. Luo. Robotwin: Dual-arm robot benchmark with generative digital twins (early version). *arXiv preprint arXiv:2409.02920*, 2024.
- [33] J. Ho, A. Jain, and P. Abbeel. Denoising diffusion probabilistic models. *Advances in neural information processing systems*, 33:6840–6851, 2020.

- [34] C. Lu, Y. Zhou, F. Bao, J. Chen, C. Li, and J. Zhu. Dpm-solver: A fast ode solver for diffusion probabilistic model sampling in around 10 steps. *Advances in Neural Information Processing Systems*, 35:5775–5787, 2022.
- [35] I. Loshchilov and F. Hutter. Decoupled weight decay regularization. *arXiv preprint arXiv:1711.05101*, 2017.

# Appendix

## .1 Implementation Details

During training, we use DDPM [33] as the noise sampler with a timestep of 100. During inference, we employ DPM-Solver [34] to accelerate denoising with timesteps set to 10. All training processes utilize the AdamW [35] optimizer, learning rate of  $1e-4$  that decays to  $1e-5$  during the final 10% of training. We adopt a fixed-step training regimen instead of fixed-epoch training. The single-task model is trained with a batch size of 128 for  $100 \times D$  steps, where  $D$  is the number of episode of training data, while the multi-task model uses a batch size of 256 for  $2 \times 10^5$  steps. The model predicts trajectories for the next 64 timesteps, while only the first 32 timesteps are used during testing.

The parameter distribution of the three models mentioned in Section. 4.6 and Tab. 1 is shown in Tab. 5.

Model	$\epsilon_{img}$	$\epsilon_{depth}$	$\epsilon_{text}$	$\epsilon_{state}$	$E_{feat}$	$E_{spatial}$	$D_{action}$	All
Single Task	28.26	0.09	0.0	5.77	0.0	0.73	14.05	47.20
Multi Task - GD	28.26	0.09	103.85	5.77	20.89	0.73	15.55	175.33
Multi Task - QW	<u>637.71</u>	0.09	-	5.77	<u>2942.98</u>	0.73	15.55	3622.01

Table 5: Model parameter counts (M). GD denotes GroundingDINO, QW represents Qwen2.5-vL. Parameters marked with underscores remain frozen during training (see Sec. 4.6).  $\epsilon$ ,  $E$ , and  $D$  denote the encoders, enhancers, and decoder respectively.

## .2 Camera Intrinsic Generalization

As described in Sec. 4.6, we employ camera intrinsic standardization to enhance the model’s intrinsic generalization capability. This technique enables image transformation to arbitrary intrinsic parameters, as demonstrated in Figure 4 which shows the conversion from L515 camera images to D435 intrinsic parameters. Note that standardization may introduce field-of-view (FOV) loss or image padding. We validate the generalization improvement brought by intrinsic standardization in Tab. 6. We train the model on D435 camera and conduct zero-shot testing on L515 camera, achieving only 6.3% success rate. When applying Camera Intrinsic Standardization, the success rate increases to 83.6%, approaching the original camera’s 84.5%, demonstrating the effectiveness of camera intrinsic standardization.

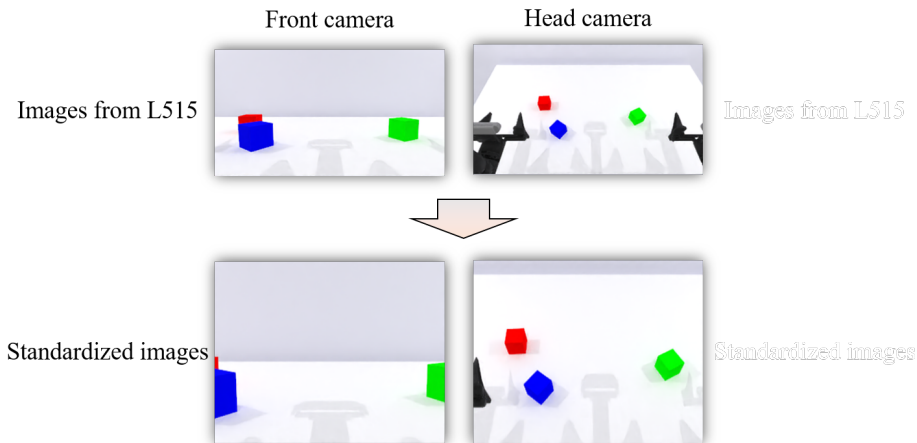


Figure 5: Example of camera intrinsic standardization, transforming L515 images to D435 intrinsic parameters.

Train	Test	CIS	Blocks Stack Hard	Dual Bottles Pick Hard	Block Handover
D435	D435		$89.7 \pm 1.7$	$60.7 \pm 0.5$	$96.7 \pm 1.2$
D435	L515		$0.0 \pm 0.0$	$7.0 \pm 2.2$	$10.3 \pm 5.2$
D435	L515	✓	$88.7 \pm 2.1$	$58.7 \pm 0.5$	$93.7 \pm 1.7$
Train	Test	CIS	Shoe Place	Empty Cup Place	Mean
D435	D435		$88.3 \pm 1.2$	$87 \pm 2.2$	$84.5 \pm 1.3$
D435	L515		$8.7 \pm 0.9$	$5.3 \pm 2.1$	$6.3 \pm 2.1$
D435	L515	✓	$87.0 \pm 0.8$	$90.0 \pm 0.8$	$83.6 \pm 1.2$

Table 6: Experimental results of camera intrinsic generalization. CIS refers to 'Camera Intrinsic Standardization'. D435 and L515 denote two different cameras.

### .3 Visualization of 3D Position Embedding

Fig. 6 illustrates the correlation between 3D position embeddings of the spatial enhancer, revealing a positive correlation between their cosine distance in feature space and Euclidean distance in 3D space.

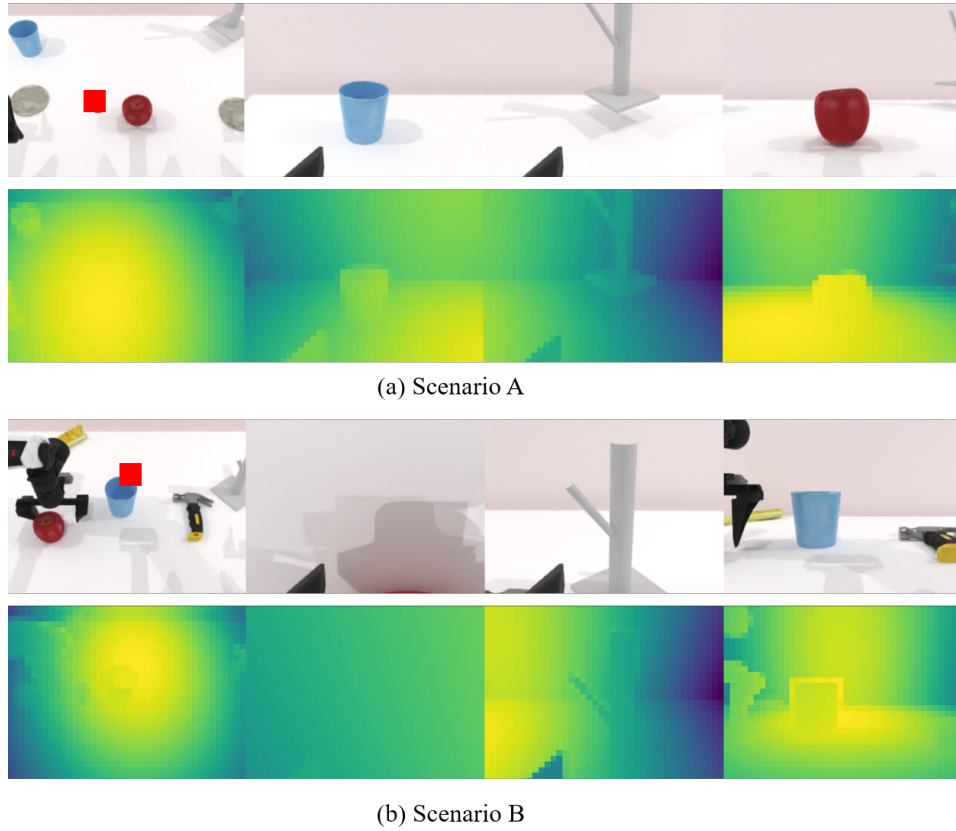


Figure 6: Visualization of 3D position embeddings. The heatmap represents the cosine distances between all position embeddings and the position embedding of the target location (red block on the images).